Journal of Materials Chemistry A

PAPER

View Article Online
View Journal

Cite this: DOI: 10.1039/c8ta00303c

A novel ball milling technique for room temperature processing of TiO_2 nanoparticles employed as the electron transport layer in perovskite solar cells and modules†

Mriganka Singh,[a] Chien-Hung Chiang,[b] Karunakara Moorthy Boopathi,[c] Chintam Hanmandlu,[c] Gang Li,[e] Chun-Guey Wu,[*bf] Hong-Cheu Lin*[a] and Chih-Wei Chu[*cdg]

Anatase titanium dioxide (an-TiO_2) is often used as the electron transporting material (ETM) in planar-heterojunction perovskite solar cells (PSCs) because of its excellent semiconductor characteristics, outstanding optical transmittance, and suitable band structure. Herein, we report an inexpensive method for mass-scale production of TiO_2 ETMs at room temperature (RT ~ 30 °C), involving the grinding of large clumps of an-TiO_2 to form a suspension of TiO_2 nanoparticles (NPs) in isopropyl alcohol for *meso*-superstructured PSCs. This process does not involve any chemical synthesis; it is a purely physical process. The lowest unoccupied molecular orbital (LUMO) of ground an-TiO_2 NPs, estimated using ultraviolet photoelectron spectroscopy (UPS), was *ca.* 4.06 eV, which is a salient feature for the active layer. A regular perovskite solar cell (PSC) based on a $CH_3NH_3PbI_3$ absorber and ground an-TiO_2 ETL exhibited a champion power conversion efficiency (PCE) of 17.43% with an active area of 0.1 cm^2. The same ground an-TiO_2 NPs were used to fabricate a large-area (designated area: 25.2 cm^2) PSC and a PCE of 14.19% was achieved. PSC devices incorporating the ground an-TiO_2 NP ETLs exhibited an attractive long-term device stability, with the PCE retaining approximately 85% of the initial values after 80 days.

Received 13th January 2018
Accepted 21st March 2018

DOI: 10.1039/c8ta00303c

rsc.li/materials-a

Introduction

Continued technological improvement of perovskite solar cells (PSCs) will require enhancements in power conversion efficiency (PCE) and stability while maintaining low material costs and ease of fabrication.[1–3] There is a vast diversity in photovoltaic (PV) technologies incorporating organic/inorganic hybrids, of the form ABX_3 (A = CH_3NH_3, Cs; B = Pb, Sb; X = Cl, Br, I), into PSCs.[4–6] The most common ABX_3 used is $CH_3NH_3PbI_3$ (methylammonium lead triiodide) perovskite which has a very high absorption coefficient (*ca.* 5.7 × 10^4 cm^{-1} at 600 nm), a long charge carrier diffusion length (>1000 nm), low exciton binding energy, and highly tunable charge carrier mobilities and band gaps.[7–11] These properties make perovskites particularly efficient in solar energy applications. Perovskite films have been fabricated in many ways, including spin-coating,[12] atomic layer deposition,[13] chemical vapor deposition,[14] and two-step interdiffusion.[15] The reported efficiencies of PSCs have reached greater than 22% within just a decade of development.[16] In general, the frameworks of PSCs fall into two categories: conventional (n–i–p)[17] and inverted (p–i–n) architectures.[18] The conventional structures can be further divided into two subcategories: mesoporous scaffolds and planar structures. For conventional PSCs, the most commonly used materials for the electron transporting layer (ETL) are titanium dioxide (TiO_2)[19] and tin(IV) oxide (SnO_2);[20] the hole transporting layer (HTL) is 2,2′,7,7′-tetrakis(*N*,*N*-di-*p*-methoxyphenylamino)-9,9′-spirobifluorene (spiro-MeOTAD).[21] The major disadvantage of incorporating barrier-layer TiO_2 (bl-TiO_2) and mesoporous-layer TiO_2 (mp-TiO_2) together in the scaffold structure is that the sintering is required at very high temperatures (≥450 °C),[17] precluding the fabrication of plastic-based flexible substrates as well as limiting the commercialization (*e.g.*, increasing the cost) of TiO_2-based PSCs. Nevertheless, TiO_2

[a]Department of Materials Science and Engineering, National Chiao Tung University, Hsinchu, Taiwan. E-mail: linhc@cc.nctu.edu.tw

[b]Research Center for New Generation Photovoltaics, National Central University, Jhong-Li, Taiwan. E-mail: t610002@cc.ncu.edu.tw

[c]Research Center for Applied Sciences, Academia Sinica, Taipei, Taiwan. E-mail: gchu@gate.sinica.edu.tw

[d]College of Engineering, Chang Gung University, Guishan District, Taoyuan City, Taiwan

[e]Department of Electronic and Information Engineering, The Hong Kong Polytechnic University, Hung Hom, Kowloon, Hong Kong, China

[f]Department of Chemistry, National Central University, Jhong-Li, Taiwan

[g]Department of Materials Science and Engineering, National Tsing Hua University, Hsinchu, Taiwan

† Electronic supplementary information (ESI) available. See DOI: 10.1039/c8ta00303c

has an excellent band alignment of its lowest unoccupied molecular orbital (LUMO; *ca.* −4.0 eV) and highest occupied molecular orbital (HOMO; *ca.* −7.2 eV), making it still a seemingly appropriate choice for devices incorporating a $CH_3NH_3PbI_3$ active layer[22] and bulk heterojunction solar cells.[23,24]

Many attempts have been made to enhance the charge separation of the perovskite absorber through interfacial modification of the TiO_2 compact layer, using for example, the small molecule ITIC,[25] carboxyl groups,[26] amino acids,[27–29] thiols,[30] graphene quantum dots,[31] colloidal quantum dots,[22] self-assembled fullerene monolayers,[32] and Li-doping.[33] These processes were attempted to strengthen the bond between the compact TiO_2 layer and the perovskite film, avoid charge recombination, and form high-quality films to achieve higher device performance. To ensure that highly compact TiO_2 layers were made, Wu *et al.* prepared TiCl–TiO_2 layers through treating TiO_2 films with $TiCl_4$ to fill any pinholes.[34] Yella *et al.* found that chemical-bath deposition of nanocrystalline rutile TiO_2 from $TiCl_4$ at low temperature (70 °C) was more efficient than spray pyrolysis of TiO_2 through high-temperature (500 °C) sintering.[35] Cojocaru *et al.* also reported high-temperature synthesized TiO_2 and $TiCl_4$ post-treatment to improve the cell performance.[36]

Furthermore, being able to fabricate a TiO_2 ETL at low temperature to achieve high efficiency regular PSCs is extremely important for reducing the cost of PSCs. Snaith's group first reported a low temperature (150 °C) processed TiO_2 ETL from TiO_2 nanoparticles (NPs) synthesized by a hydrothermal method. In that method, a titanium(IV) isopropoxide compound was used as a starting material, which required many wetting agent (acetic acid, deionized water, and nitric acid).[37] Later, many reports focussed on low temperature (150 °C) processed TiO_2 prepared through non-hydrolytic sol–gel techniques.[19,22,38,39] In non-hydrolytic sol–gel techniques $TiCl_4$ was used as a precursor and the reaction required rigorous synthesis procedures with a large number of surfactants (ethanol, benzyl alcohol, and diethyl ether) and extra titanium bis(acetyl acetonate)dichloride is needed for stabilizing the formed TiO_2 NPs.[39] One of the major drawbacks of low temperature processed TiO_2 is that it's not suitable for flexible substrates like polyethylene terephthalate (PET), which cannot withstand annealing temperatures higher than 120 °C. Therefore, it is highly useful to develop a method for the fabrication of efficient TiO_2 ETLs, which can be easily processed at an ambient temperature without any further annealing.

To realize ambient processing of TiO_2 ETLs without $TiCl_4$-treatment and avoid the degradation of TiO_2 to TiO_x in PSCs remain a challenge. In this paper, for the first time we demonstrate a simple ball milling method for the synthesis of anatase TiO_2 (an-TiO_2) at room temperature (RT ∼ 30 °C) for fabricating TiO_2 compact layers. Our method for the production of TiO_2 ETLs involves grinding a large clump of an-TiO_2 with zirconium dioxide (zirconia; ZrO_2) beads in isopropyl alcohol (IPA) to achieve a suspension of an-TiO_2 NPs (G-TiO_2 NPs). The TiO_2 ETL made from G-TiO_2 NPs is very dense with a low number of pinholes, allowing the electrons to move from the active layer to the electrode. To test the feasibility of these G-TiO_2 NPs, a PSC based on the ETL (*i.e.*, without any doping) prepared from G-TiO_2 NPs was tested. Furthermore, we are aware that there are many avenues (*e.g.*, doping or introducing another ETL layer on the top of G-TiO_2) available to obtain very smooth, pinhole-free surfaces to ensure hysteresis-free cell or to improve power conversion efficiencies (PCEs) of the cell. Here we compare only the performances of a low-temperature processed G-TiO_2 film, sol–gel TiO_2 (S-TiO_2) compact layer and S-TiO_2 plus mesoporous TiO_2 layer, the latter two were heated at 450 °C. Most notably, G-TiO_2 NPs were processed at low temperature (<150 °C), they are compatible with ITO or other plastic-based flexible substrates; in contrast, S-TiO_2 and mesoporous TiO_2 films were made at high temperature (450 °C), meaning that FTO was the only choice as the substrate. Therefore the structure of the PSC reported in this paper is ITO (or FTO)/G-TiO_2 (or S-TiO_2)/$CH_3NH_3PbI_3$/spiro-MeOTAD/MoO_3/Ag.

Experimental

Materials

Anatase titanium dioxide (TiO_2) powder (99.7%; Nanostructured and Amorphous Materials, Los Alamos, New Mexico, USA), zirconium dioxide (ZrO_2, zirconia) beads (density: 5.95 g cm^{-3}; size: 100 μm; Oriental Cera TEC., Taiwan), lead iodide (PbI_2, 99.9%; Alfa Aesar), methyl ammonium iodide (MAI; UR Company, Taiwan), 2,2′,7,7′-tetrakis(*N*,*N*-di-*p*-methoxyphenylamino)-9,9′-spirobifluorene (spiro-MeOTAD; Luminescence Technology, Taiwan), bis(trifluoromethane)sulfonimide lithium salt (Li-TFSI, 99%; UR Company, Taiwan), and 4-*tert*-butylpyridine (TBP, 96%) were obtained from their noted suppliers. Isopropyl alcohol (IPA), *N*,*N*-dimethylformamide (DMF), acetonitrile (ACN), and chlorobenzene (CB) were purchased from Sigma-Aldrich. All materials and solvents were used without further purification.

TiO_2 nanoparticle (G-TiO_2 NP) preparation with a ball milling method

Anatase TiO_2 powder was mixed with IPA to form a suspension at a concentration of 5 wt%; micro zirconia beads (*ca.* 600 g) were added and then the mixture was transferred to the chamber of a grinder. The grinder was placed into a dispersing machine (AG-1000, Allgen Technology). An electric stirrer was attached to the dispersing machine. The grinding process was performed with a rotation speed of 2000 rpm for 360 min at room temperature. After 6 h, the suspension has a milky color; an independent layer on the top of zirconia beads was evident to the naked eye. The upper layer of TiO_2 NPs was separated; the residue from the zirconia beads settled to the bottom of the chamber because of its higher density. The final concentration of the ground TiO_2 (G-TiO_2 NPs) paste was 3 wt%.

Device fabrication

Patterned FTO (or ITO) substrates (<10 Ω cm^{-1}, RiT display) were cleaned with detergent, rinsed with deionized (DI) water, and sonicated in acetone and isopropyl alcohol. The substrates were blown dry under N_2 and stored in an oven, at least overnight. The cleaned and dried substrates were treated in a UV/ozone cleaner for 15 min to remove any contaminants and to

make the FTO substrates more hydrophilic. The ground TiO_2 suspension (1.5 wt%) was sonicated (*ca.* 20–30 min) prior to spin-coating on the ozone-treated substrates. The G-TiO_2 film (*ca.* 80 nm) was prepared using spin-coating (4000 rpm, 30 s) through solution processing, followed by annealing (30–100 °C) for 30 min. The G-TiO_2 film functions as a compact layer as well as a mesoporous layer. $TiCl_4$ (33.8 μL/3 mL in ethanol) was used to prepare the compact TiO_2 film (S-TiO_2) *via* a sol–gel process, by spin-coating at 3000 rpm, 30 s followed by sintering at a high-temperature of 450 °C for 30 min. For mesoporous TiO_2 (*m*-TiO_2) layer deposition we used a commercially available TiO_2 paste (Dyesol) in ethanol, which was deposited by spin-coating at 3000 rpm, 30 s, dried at 120 °C and then sintered at 450 °C according to the literature report.[40] The perovskite layer was deposited using a two-step process. For deposition of the perovskite absorber and the HTL, PbI_2 (45 wt%) and KCl (1 wt%) dissolved in DMF, MAI (1 wt%) in 2-propanol, and spiro-MeOTAD (5 wt%) in CB with the additives LiTFSI (90 mg/530 μL in ACN; 40 μL) and TBP (10 μL) were used. All solutions were stirred overnight at 70 °C. The PbI_2 solution was spin-coated (3000 rpm, 30 s) on both types of TiO_2 ETL and annealed at 100 °C, 5 min under N_2 to form a crystalline film. The MAI layer was then spin-coated (3000 rpm, 30 s) on top of the PbI_2 film and annealed (135 °C, 15 min) to form the perovskite (300 nm) film. Finally, spiro-MeOTAD (120 nm) was coated (3000 rpm, 30 s) on the perovskite without annealing. Followed by the deposition of MoO_3 and Ag electrodes at thicknesses of 8 and 80 nm, respectively. The deposition and annealing processes of the active layer and HTL were performed under a N_2 atmosphere.

Characterization

The nanostructures and sizes of the TiO_2 nanoparticles (G-TiO_2 NPs) prepared by a ball milling method were measured using a transmission electron microscope (TEM, JEM-2100F, JEOL) and a particle size analyzer (Brookhaven 90Plus Sn11408). Ultraviolet photoelectron spectroscopy (UPS, PHI 5000 Versa Probe) was performed to measure the valence band maximum (VBM), using He(I) emission (21.22 eV, *ca.* 50 W) as the source of ultra-violet light. X-ray photoelectron spectroscopy (XPS, PHI 5000 Versa Probe) was performed with an Al Kα X-ray source (1486.6 eV). Scanning electron microscopy (SEM) was performed using an FEI Nova 200 microscope (15 kV). Atomic force microscopy (AFM) was performed using a Bruker Dimension Icon atomic force microscope. G-TiO_2 (or S-TiO_2) films spin-coated on ITO (or FTO) substrates were used for SEM and AFM measurements. Absorption spectra of the films were measured using a Jacobs V-670 UV-vis spectrophotometer. The devices were illuminated with a solar simulator (Thermal Oriel 1000 W), which provided a simulated AM 1.5 spectrum (100 mW cm^{-2}), inside a glovebox, using a Xe lamp. The solar cell testing was performed by using a mask. The dimension of the mask is 0.1 × 0.2 cm^2 for small-area cells and for large-area sub-modules, 9 cells connected in series, the area of each cell is 0.8 × 0.35 cm^2. The light intensity was calibrated using a mono-silicon photodiode with a KG-5 color filter (Hamamatsu). The devices were encapsulated before recording their external quantum efficiency (EQE) spectra. EQE spectra were measured under monochromatic illumination (Enlitech, QE-R3011); the light output from the monochromator was focused on the photovoltaic cell being tested. The photoluminescence (PL) spectra of the $CH_3NH_3PbI_3$ thin films were measured using an optical microscope system (UniRAM, Protrustech). For the PL experiments, the wavelength of the excitation is 405 nm and all measurements were performed at room temperature.

Results and discussion

The schematic representation of the preparation of the G-TiO_2 NPs is presented in Fig. 1a. In this high-energy wet-milling grinding method, a large clump of an-TiO_2 is subjected to physical processing (without any chemical synthesis) in the presence of only zirconia beads and isopropyl alcohol to achieve a suspension of G-TiO_2 NPs. Our group has previously employed the same strategy to prepare TiO_2 NPs for bulk heterojunction organic photovoltaics.[23] This simple grinding process requires inexpensive materials and is a facile approach for the production of large amounts of TiO_2 NPs. Fig. 1b displays a photograph of massive production of G-TiO_2. Fig. 1c presents the complete device architecture (glass/ITO/G-TiO_2/$CH_3NH_3PbI_3$/spiro-MeO-TAD/MoO_3/Ag); Fig. 1d displays a cross-sectional scanning electron microscopy (SEM) image which reveals an approximately 80 nm-thick G-TiO_2 NP ETL present beneath the perovskite layer.

Transmission electron microscopy (TEM) images were taken to obtain crystallographic information about the pristine an-TiO_2 and the ground an-TiO_2 (G-TiO_2 NPs). Fig. 2a presents a bright-field TEM image of the pristine an-TiO_2 powder; the inset displays the corresponding electron diffraction pattern. The TEM image reveals large clumps of morphology and the diffraction pattern features a spotty ring confirming high crystallinity. A bright-field TEM image of the ground an-TiO_2 (G-TiO_2 NPs) displayed in Fig. 2b reveals that after physical processing the TiO_2 turns into NPs. Fig. 2c presents the selective-area electron diffraction pattern of the G-TiO_2 NPs; the weak intensity of the polymorphic ring suggests that the grinding process reduces the crystallinity of TiO_2. The change in crystallinity of TiO_2 after grinding was also evident in the phase contrast or Moiré patterns. High-resolution transmission electron microscopy (HRTEM) image (displayed in Fig. 2d) revealed the crystal lattice spacing and interplanar distances expected for TiO_2 in an anatase phase. This anatase phase featured many lattices, with a *d*-spacing of approximately 0.312 nm representing the interplanar distances of the (1 0 1) planes, consistent with literature data.[22] The inset of Fig. 2d presents the fast Fourier transform (FFT) pattern of the HRTEM image of the G-TiO_2 NPs. To determine the average particle sizes of G-TiO_2 NPs, we performed dynamic light scattering (DLS) and atomic force microscopy (AFM) measurements. Fig. S1 (of the ESI†) shows the average particle size (nm) of the TiO_2 powder with respect to the grinding time (1–6 h); the average particle size decreased upon increasing the grinding time to 6 h: the large clumps of TiO_2 disaggregate quickly into smaller particles. The inset picture in Fig. S1† provides evidence of the dispersion of TiO_2

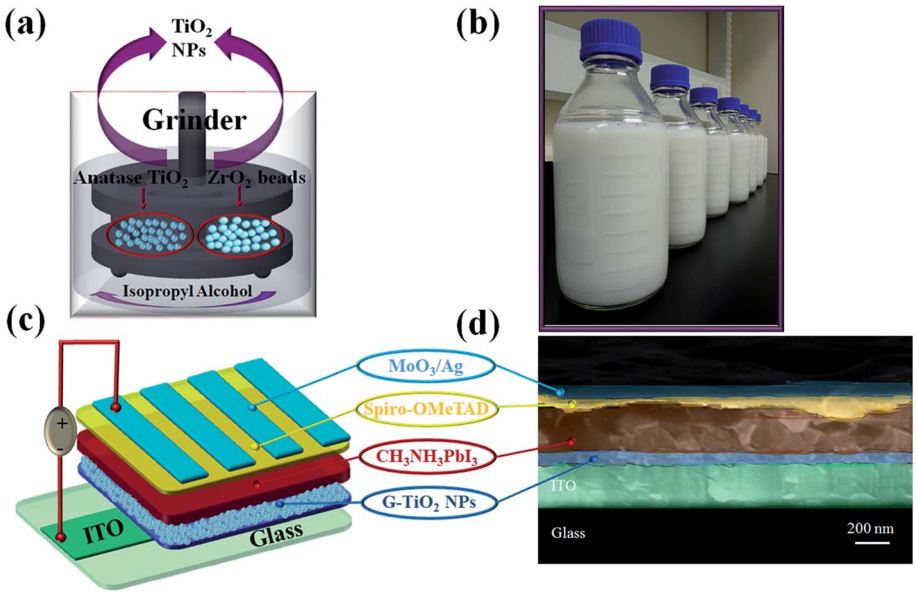

Fig. 1 (a) Schematic representation of the procedure used to prepare G-TiO_2 NPs. (b) Photograph revealing the capability of producing massive amounts (bottle size: 1 L) of the G-TiO_2 suspension. (c) Schematic representation of the device architecture: glass/ITO/G-TiO_2 NPs/$CH_3NH_3PbI_3$/spiro-MeOTAD/MoO_3/Ag. (d) Cross-sectional SEM image of a device having the structure depicted in (c).

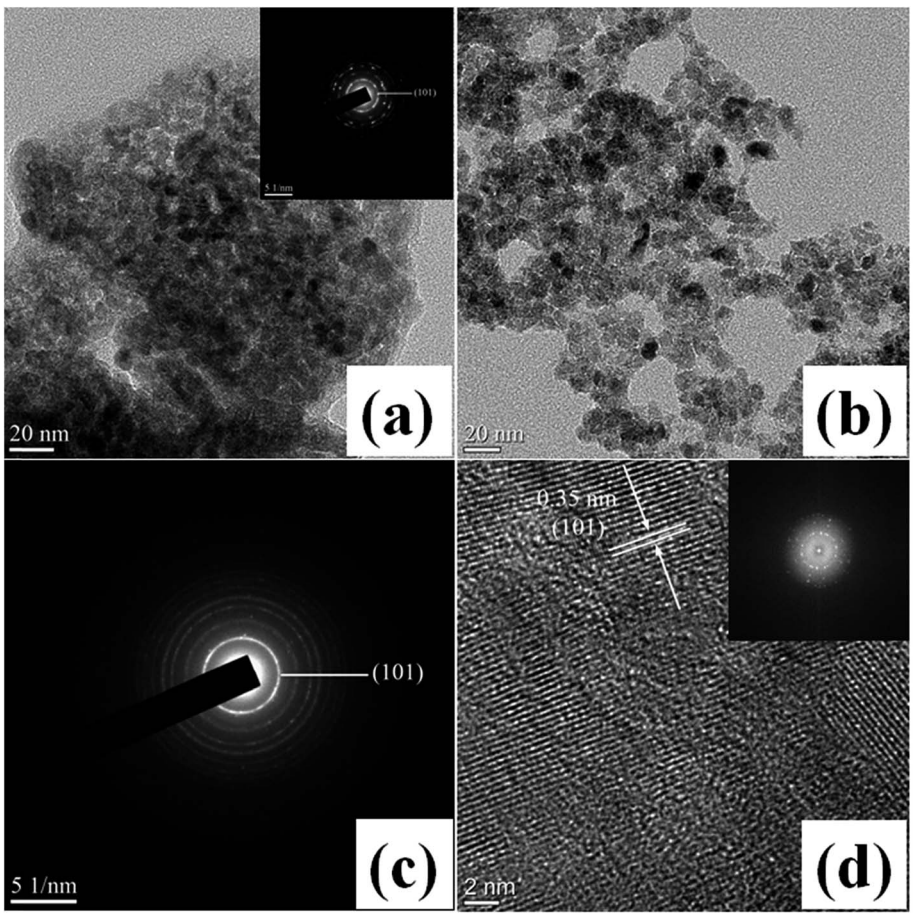

Fig. 2 (a) Bright-field TEM image of pristine an-TiO_2 powder; inset: corresponding diffraction pattern. (b) Bright-field TEM image of the ground TiO_2 (G-TiO_2 NPs). (c) Selective area diffraction pattern of G-TiO_2 NPs with the (101) orientation. (d) HRTEM image of G-TiO_2 NPs; inset: the corresponding FFT pattern.

NPs after grinding (these pictures were taken after the suspension stands for 4 days). Fig. S2, ESI† presents the AFM image of a thin G-TiO_2 film made by spin-coating the G-TiO_2 NP suspension onto an ITO substrate; the average particle size of the G-TiO_2 NPs was approximately 20–30 nm, with a root-mean-square (RMS) roughness of 5.46 nm.

Planar heterojunction PSCs having the architecture of ITO (or FTO)/G-TiO_2 (or S-TiO_2)/$CH_3NH_3PbI_3$/spiro-MeOTAD/MoO_3/Ag were fabricated and the current density–voltage (J–V) curve of the cells measured under simulated AM 1.5G illumination (100 mW cm^{-2}) is illustrated in Fig. 3a. The champion performance of the device incorporating a G-TiO_2 ETL, fabricated using a low-temperature process, exhibited a short-circuit photo current density (J_{sc}) of 21.7 mA cm^{-2}, an open-circuit voltage (V_{oc}) of 1.07 V, and a fill-factor (FF) of 0.75, yielding a PCE (η) of 17.4% with an average PCE of 14.4%; the champion device incorporating S-TiO_2 ETL exhibited the J_{sc}, V_{oc}, and FF values of 20.0 mA cm^{-2}, 1.02 V, and 60.3%, respectively, yielding a PCE (η) of 12.3% with an average PCE of 10.8%. We also fabricated a cell with a mesoporous TiO_2 (m-TiO_2) film on S-TiO_2 having the architecture of FTO/S-TiO_2/m-TiO_2 (150 nm)/$CH_3NH_3PbI_3$/spiro-MeOTAD/MoO_3/Ag. The cell exhibited a PCE of 18.2% (J_{sc} = 21.4 mA cm^{-2}; V_{oc} = 1.1 V; FF = 0.77) in the reverse scan direction and in the forward scan direction the PCE is only 13.9% (the corresponding J–V curve is displayed in Fig. S3 (ESI†)). Fig. S4 (ESI†) presents J–V curves for G-TiO_2 and S-TiO_2 based cells in the reverse and forward scan directions and the detailed PV performance is mentioned in Table S1 (ESI†). It is clearly shown that the S-TiO_2 cell suffers from huge hysteresis, which may be due to higher trap density in the ETL. The J–V curve for G-TiO_2 based PSCs shows less hysteresis at delay times ranging from 3 ms to 1000 ms as the data shown in Fig. S5 (ESI†).

The higher PCE of the G-TiO_2-based device indicates that the G-TiO_2 film can block the leakage current or extract the electrons more effectively compared to that of the S-TiO_2 ETL. Fig. 3b presents the photocurrent density–voltage (J–V) and external quantum efficiency (EQE) curves of the best PSCs incorporating G-TiO_2 and S-TiO_2 ETLs. The spectral sensitivity wavelengths spanned from the visible to the near-IR region (*ca.* 300–800 nm) with peak EQEs of approximately 85 and 80% for G-TiO_2 and S-TiO_2 based PSCs, respectively. The large spectral response range suggests that, for both devices, it was easy to convert the incident photons to charges even at long wavelengths. Fig. 3c presents the PV performance of a large-area (designated area: 25.2 cm^2) solar submodule (displayed in Fig. S6, ESI†) incorporating G-TiO_2 as the ETL. The champion sub-module displayed a short-circuit photocurrent (I_{sc}) of 55.21 mA, V_{oc} of 9.12 V, and FF of 71%, yielding a PCE (η) of 14.19%. The stability of the planar-heterojunction PSCs incorporating G-TiO_2 and S-TiO_2 as the ETLs, measured under a N_2 environment, is shown in Fig. 3d (the corresponding variations in the J_{sc}, V_{oc}, and FF values *vs.* time are presented in Fig. S7, ESI†). The PCE of the S-TiO_2-based PSCs decreases to less than 50% of the initial value after 40 days of storage; in contrast, the G-TiO_2-based PSC devices had excellent stability, retaining approximately 85% of their initial PCE after standing for 80 days. Fig. S8, ESI† presents the histograms of the performance (J_{sc}, V_{oc}, FF, and PCE) of 51 individual G-TiO_2 and S-TiO_2-based devices measured

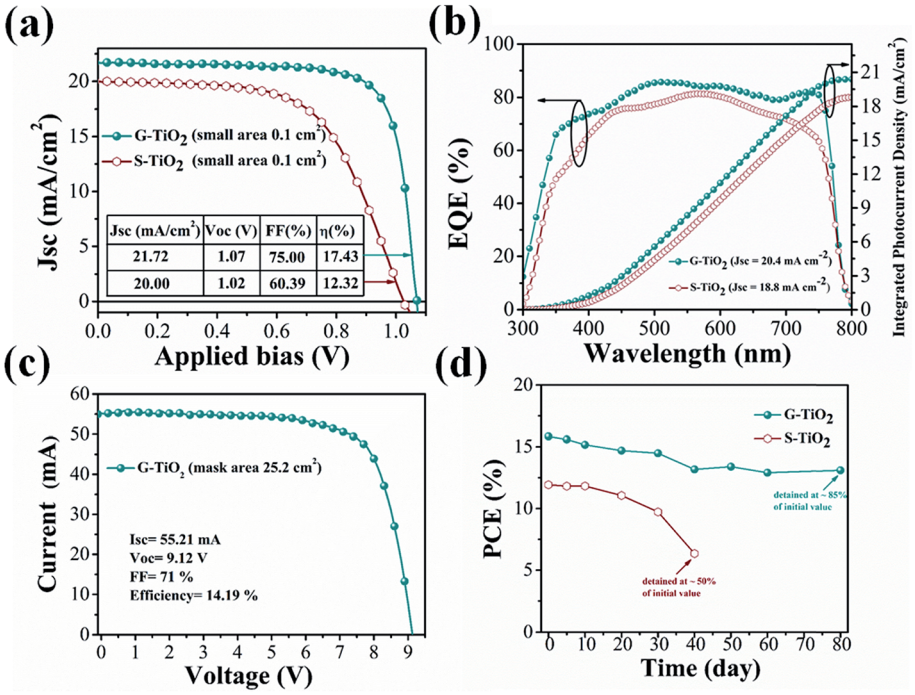

Fig. 3 (a) J–V curves of the best devices having the structure ITO (or FTO)/G-TiO_2 (or S-TiO_2)/$CH_3NH_3PbI_3$/spiro-MeOTAD/MoO_3/Ag, measured in the reverse scan direction under AM 1.5G sunlight illumination (intensity: 100 mW cm^{-2}). (b) EQE response spectra of the G-TiO_2 and S-TiO_2-based champion cells and the corresponding integrated current densities. (c) I–V curve for large-area (designated area: 25.2 cm^2) solar submodules incorporating G-TiO_2 ETLs. (d) Long-term stability of the best cell using a G-TiO_2 or S-TiO_2 ETL stored in a glovebox under N_2.

under AM 1.5G white light illumination (100 mW cm^{-2}). The photovoltaic parameters for best cells and sub-modules based on low temperature processed G-TiO_2, and high-temperature S-TiO_2 films prepared in this study as the electron transporting layers are summarized in Table 1. Tables S2 and S3 (ESI†) list the device performance of PSCs (small-area: ≤0.1 cm^2) based on low-temperature TiO_2 ETLs prepared with various deposition methods and the efficiency of the perovskite solar submodules with various areas based on a TiO_2 ETL prepared at various temperatures, respectively reported previously.

Fig. 4a presents the ultraviolet photoelectron spectra [He(I)] of G-TiO_2 and S-TiO_2 films. Signals for two photoelectrons appear in the UPS range. The primary photoelectron (upper emission) cut-off energies (E_f) of the G-TiO_2 and S-TiO_2 films were 16.70 and 16.54 eV, respectively; the secondary photoelectron (lower emission) onset energies (E_i) were 2.68 and 2.34 eV, respectively. We calculated the HOMO energies of these TiO_2 film using eqn (1):[24,41]

$$\Phi = h\nu - (E_f - E_i) \quad (1)$$

where $h\nu$ (=21.2 eV) is the incident photon energy for He(I). The valence band energies of G-TiO_2 and S-TiO_2 were −7.18 and −7.0 eV, respectively. These estimated values are consistent with those reported previously.[42] Meanwhile, according to the Tauc formula for a direct band gap semiconductor,[43] the optical band gap energies (E_g) of G-TiO_2 and S-TiO_2 were 3.13 and 3.01 eV, respectively (estimated from the UV-vis absorption spectra presented in Fig. S9, ESI†). Thus, the conduction band (CB) energies of G-TiO_2 and S-TiO_2 determined from the valence band maximum (VBM) were −4.05 and −3.99 eV, respectively as the diagram displayed in Fig. 4b. We also employed X-ray photoelectron spectroscopy (XPS) to examine the change in the surface oxidation state as well as the optical band gap of G-TiO_2 and S-TiO_2. Fig. 4c and d present the Ti 2p and O 1s core-level binding energy of G-TiO_2 and S-TiO_2, respectively. The Ti $2p_{1/2}$ and Ti $2p_{3/2}$ peaks for G-TiO_2 appeared at the binding energies of 465.3 and 459.4 eV, respectively; for S-TiO_2, these peaks appeared at binding energies of 465 and 459.2 eV, respectively, no significant difference between the two types of TiO_2 films. In the O 1s spectra of G-TiO_2 and S-TiO_2 films, peaks appeared at binding energies of 530.8 and 530.6 eV, respectively. It seems that Ti in both G-TiO_2 and S-TiO_2 films primarily feature the Ti^{4+} oxidation state.[44]

The morphology, roughness, and surface coverage of the perovskite absorber (besides the ETLs) play vital roles in the performance of planar-heterojunction solar cells. SEM images of both TiO_2 ETLs displayed in Fig. 5a and c reveal that the surface coverage of the G-TiO_2 film is better than that of the S-TiO_2 film, but the corresponding AFM images (illustrated in Fig. S10, ESI†) showed that the RMS roughness of the S-TiO_2 film (3.69 nm) was less than that of the G-TiO_2 film (9.97 nm). The SEM images of the perovskite films shown in Fig. 5b and d, evidence that the grain size of the perovskite film deposited on G-TiO_2 is approximately 200–300 nm which is bigger than that of the perovskite film deposited on S-TiO_2 (the RMS values of the perovskite films deposited on G-TiO_2 and S-TiO_2 films are 45.6 nm and 35.3 nm, respectively obtained from the AFM data displayed in Fig. S10, ESI†).[45] Moreover, perovskite films deposited on S-TiO_2 had more pinholes and higher non-uniformity in the grain size, which are the disadvantageous for PV applications compared to the perovskite film on G-TiO_2.

It seems that the roughness of the TiO_2 ETL will affect the quality of the perovskite film and therefore the photovoltaic performance of the corresponding cells. However, a characteristic of the low temperature TiO_2 film is the difficulty in tuning the porosity of the low-temperature TiO_2 film to improve the cell performance since no polymer was added to the G-TiO_2 NP paste and no high temperature sintering of the spin-coated G-TiO_2 film was performed. In this work, we had tried to prepare a G-TiO_2 layer with various thicknesses by using different concentrations of the G-TiO_2 NP suspension and the optimal thickness (80 nm) was found as in the data shown in Fig. S11 (ESI†). Furthermore, without post film treatment, the grain size of perovskite films deposited on a low-temperature TiO_2 ETL is generally small (200–700 nm), according to the research groups.[35,46,47] The grain size of the perovskite film prepared by us falls in this size range. However, the PCE of our regular cell based on a G-TiO_2 ETL is slightly higher than the other reported data.[35,46,47] It is due to the good quality (high conductivity since contains no other additive) of the G-TiO_2 film prepared by our method.

Conventional PSCs exhibit current hysteresis sometimes. A common reason for *J–V* hysteresis is a high trap-density in the perovskite absorber.[48] Here, we performed dark current–voltage (*I–V*) measurements (Fig. 6) to calculate the electron trap-state density in the electron-only devices [ITO (or FTO)/G-TiO_2 (or S-TiO_2)/$CH_3NH_3PbI_3$/PCBM/Ag]. Linear relationships (ohmic responses) appeared for both electron-only devices at low bias voltage. The rapid non-linear increase in current occurs when the bias voltage surpassed the kink point, illustrating the point at which the trap-states were fully filled. The trap-state density was calculated from the trap-filled limit voltage (V_{TFL}) using eqn (2).[49]

Table 1 PV performance of PSCs having the structure ITO (or FTO)/G-TiO_2 (or S-TiO_2)/$CH_3NH_3PbI_3$/spiro-MeOTAD/MoO_3/Ag, measured under AM 1.5G illumination

Device structure	PCE (%)	V_{oc} (V)	J_{sc} (mA cm^{-2})	I_{sc} (mA)	FF (—)
G-TiO_2 (cell)	17.43	1.07	21.72	—	0.75
G-TiO_2[a] (cell)	14.39 ± 1.19	1.00 ± 0.02	21.60 ± 1.14	—	0.66 ± 3.5
G-TiO_2 (module)	14.19	9.12	—	55.21	0.71
S-TiO_2 (cell)	12.32	1.02	20.00	—	0.60
S-TiO_2[a] (cell)	10.80 ± 1.19	0.93 ± 0.01	21.34 ± 0.77	—	0.54 ± 4.2

[a] Average and standard deviation of the PV performance for 51 individual devices.

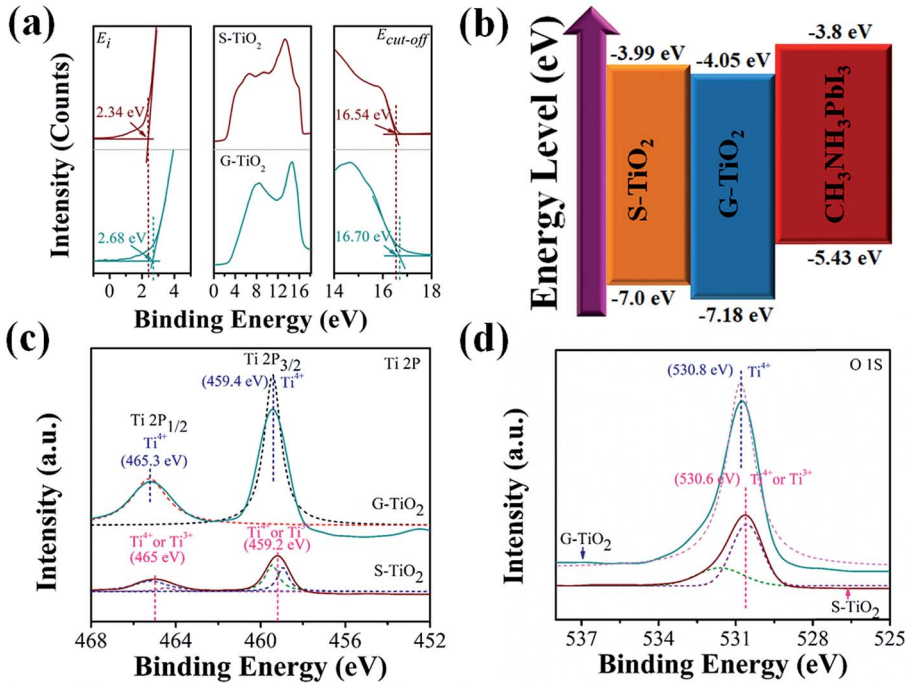

Fig. 4 (a) UPS [He(I)] spectra of G-TiO_2 (dark cyan) and S-TiO_2 (burgundy) films, with their cut-off ($E_{cut-off}$) and onset (E_i) energy boundaries. (b) Schematic representation of the HOMO and LUMO energy levels of S-TiO_2, G-TiO_2, and $CH_3NH_3PbI_3$. (c and d) XPS spectra of a G-TiO_2 ETL and S-TiO_2 ETL ((c) Ti $2p_{1/2}$ and Ti $2p_{3/2}$ spectra (d) O 1s spectra).

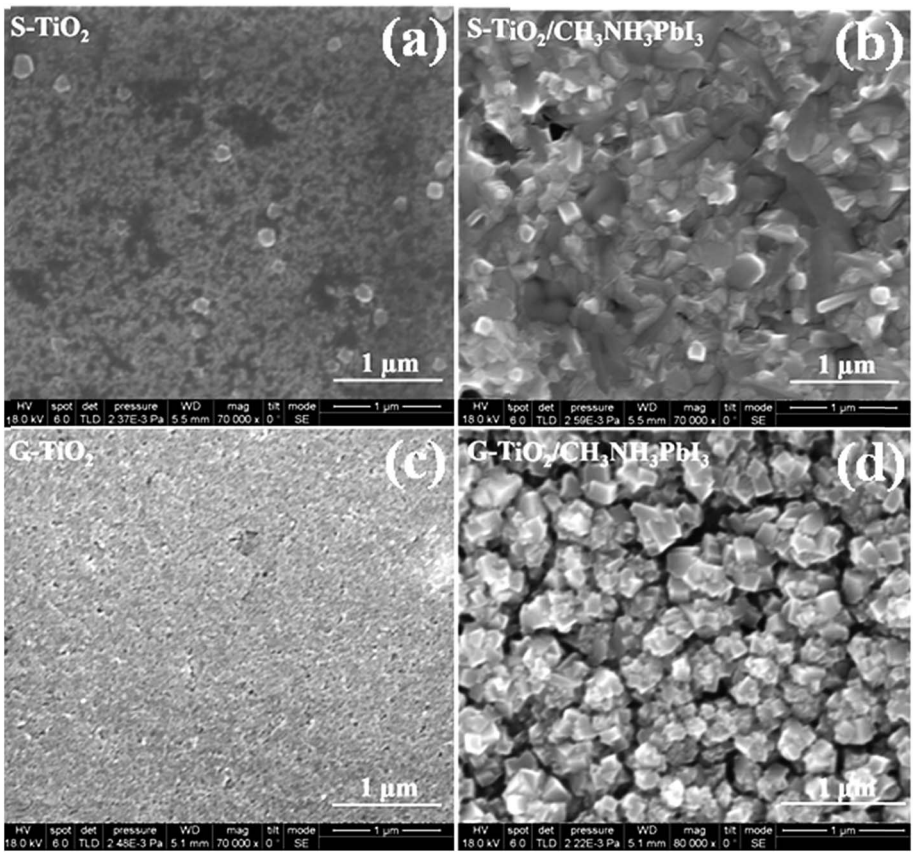

Fig. 5 SEM Surface topography images of (a) glass/FTO/S-TiO_2, (b) glass/FTO/S-TiO_2/$CH_3NH_3PbI_3$, (c) glass/ITO/G-TiO_2, and (d) glass/ITO/G-TiO_2/$CH_3NH_3PbI_3$ films.

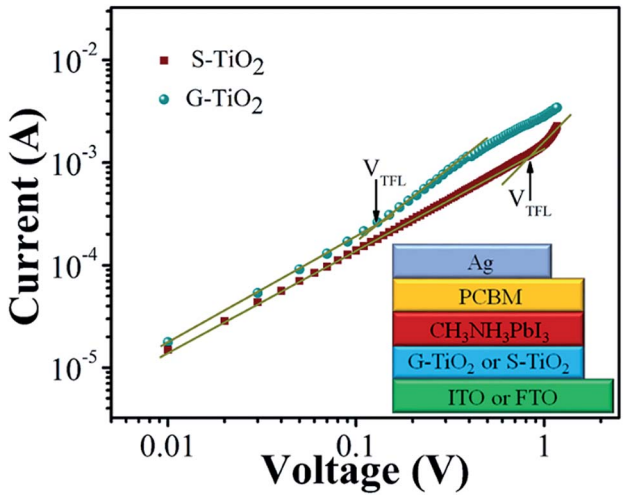

Fig. 6 Trap-density measurements of electron only devices having the structure glass/ITO (or FTO)/G-TiO_2 (or S-TiO_2)/$CH_3NH_3PbI_3$/PCBM/Ag.

$$V_{TFL} = \frac{en_tL^2}{2\varepsilon\varepsilon_0} \quad (2)$$

where e is the elementary charge of the electron, n_t is the trap-state density, L is the perovskite absorber thickness (300 nm), ε (=28.8)[50] is the relative dielectric constant of the perovskite absorber, and ε_0 is the vacuum permittivity.

The values of V_{TFL} of the S-TiO_2 and G-TiO_2 based devices were 0.82 and 0.13 V, respectively. Consequently, the trap-state density of the perovskite absorber on S-TiO_2 was 8.7 $\times$ 10^{16} cm^{-3}, in good accordance with existing studies.[51] The trap-state density of the perovskite deposited on G-TiO_2 decreased to 1.38 $\times$ 10^{16} cm^{-3} evidenced by the better film quality. Steady-state photoluminescence (PL) data can reveal the charge transport/extraction properties of the two types of TiO_2 ETLs. Fig. 7 displays the PL spectra of the perovskite films deposited on the G-TiO_2 and S-TiO_2 films. A strong PL emission peak appeared at a wavelength of approximately 775 nm, the characteristic band-edge emission of the $CH_3NH_3PbI_3$ perovskite. The S-TiO_2/perovskite exhibited a relatively higher PL intensity than the G-TiO_2/perovskite, indicating that faster electron transport from the perovskite or extraction of electrons from the perovskite to G-TiO_2 compared to S-TiO_2,[52–54] which may due to more rough G-TiO_2 and bigger perovskite grains formed on G-TiO_2 ETL.

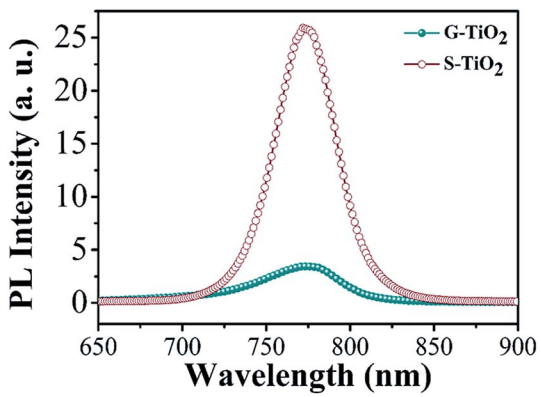

Fig. 7 Steady-state PL spectra of perovskite ($CH_3NH_3PbI_3$) films deposited on G-TiO_2 and S-TiO_2.

Conclusions

We have prepared G-TiO_2 NPs by a ball milling method for planar PSCs. The advantages of ball-milling method are reproducibility, large scale production, a cheap process and a low amount of additive (only IPA) was used for preparing TiO_2 NPs. TEM, DLS, and AFM analyses revealed that the average particle size of the G-TiO_2 NPs was 20–30 nm. The PSC cell based on the G-TiO_2 ETL (from low temperature (<150 °C) processed G-TiO_2 NPs) achieves the best PCE of 17.43% for small area cells and 14.19% for the submodule (designated area: 25.2 cm^2). PSCs incorporating a G-TiO_2 film as an ETL retained approximately 85% of their initial PCE after standing for 80 days. G-TiO_2 NPs made at low temperature were proved to be a promising material for use in PV devices such as regular perovskite solar cells.

Conflicts of interest

The authors declare no competing financial interests.

Acknowledgements

C. G. W. thanks the Ministry of Science and Technology (MOST), Taiwan, ROC (grants NSC104-2113-M-008-002-MY3 and 106-2731-M-008-004-MY2) for financial support. H. C. L. thanks the MOST of Taiwan (grants MOST 103-2113-M-009-018-MY3 and MOST 103-2221-E-009-215-MY3) for financial support. C. W. C. thanks the MOST of Taiwan (grants 104-2221-E-001-014-MY3 and 104-2221-E-009-096-MY3) and the Career Development Award of Academia Sinica, Taiwan (103-CDA-M01), for financial support.

References

1 M. A. Green, A. Ho-Baillie and H. J. Snaith, *Nat. Photonics*, 2014, **8**, 506–514.
2 N.-G. Park, M. Grätzel, T. Miyasaka, K. Zhu and K. Emery, *Nat. Energy*, 2016, **1**, 16152.
3 Y. Zhao and K. Zhu, *Chem. Soc. Rev.*, 2016, **45**, 655–689.
4 J.-H. Im, C.-R. Lee, J.-W. Lee, S.-W. Park and N.-G. Park, *Nanoscale*, 2011, **3**, 4088–4093.
5 A. Kojima, K. Teshima, Y. Shirai and T. Miyasaka, *J. Am. Chem. Soc.*, 2009, **131**, 6050–6051.
6 B. Saparov, F. Hong, J.-P. Sun, H.-S. Duan, W. Meng, S. Cameron, I. G. Hill, Y. Yan and D. B. Mitzi, *Chem. Mater.*, 2015, **27**, 5622–5632.
7 J. M. Ball, M. M. Lee, A. Hey and H. J. Snaith, *Energy Environ. Sci.*, 2013, **6**, 1739–1743.
8 V. Gonzalez-Pedro, E. J. Juarez-Perez, W.-S. Arsyad, E. M. Barea, F. Fabregat-Santiago, I. Mora-Sero and J. Bisquert, *Nano Lett.*, 2014, **14**, 888–893.

9 S. D. Stranks, G. E. Eperon, G. Grancini, C. Menelaou, M. J. Alcocer, T. Leijtens, L. M. Herz, A. Petrozza and H. J. Snaith, *Science*, 2013, **342**, 341–344.
10 Y. Wang, Y. Zhang, P. Zhang and W. Zhang, *Phys. Chem. Chem. Phys.*, 2015, **17**, 11516–11520.
11 G. Xing, N. Mathews, S. Sun, S. S. Lim, Y. M. Lam, M. Grätzel, S. Mhaisalkar and T. C. Sum, *Science*, 2013, **342**, 344–347.
12 M. M. Lee, J. Teuscher, T. Miyasaka, T. N. Murakami and H. J. Snaith, *Science*, 2012, **338**, 643–647.
13 B. R. Sutherland, S. Hoogland, M. M. Adachi, P. Kanjanaboos, C. T. Wong, J. J. McDowell, J. Xu, O. Voznyy, Z. Ning and A. J. Houtepen, *Adv. Mater.*, 2015, **27**, 53–58.
14 Q. Chen, H. Zhou, Z. Hong, S. Luo, H.-S. Duan, H.-H. Wang, Y. Liu, G. Li and Y. Yang, *J. Am. Chem. Soc.*, 2013, **136**, 622–625.
15 Z. Xiao, C. Bi, Y. Shao, Q. Dong, Q. Wang, Y. Yuan, C. Wang, Y. Gao and J. Huang, *Energy Environ. Sci.*, 2014, **7**, 2619–2623.
16 D. Bi, C. Yi, J. Luo, J.-D. Décoppet, F. Zhang, S. M. Zakeeruddin, X. Li, A. Hagfeldt and M. Grätzel, *Nat. Energy*, 2016, **1**, 16142.
17 W. S. Yang, J. H. Noh, N. J. Jeon, Y. C. Kim, S. Ryu, J. Seo and S. I. Seok, *Science*, 2015, **348**, 1234–1237.
18 I. J. Park, M. A. Park, D. H. Kim, G. D. Park, B. J. Kim, H. J. Son, M. J. Ko, D.-K. Lee, T. Park and H. Shin, *J. Phys. Chem. C*, 2015, **119**, 27285–27290.
19 H. Tan, A. Jain, O. Voznyy, X. Lan, F. P. G. de Arquer, J. Z. Fan, R. Quintero-Bermudez, M. Yuan, B. Zhang and Y. Zhao, *Science*, 2017, **355**, 722–726.
20 G. Yang, H. Lei, H. Tao, X. Zheng, J. Ma, Q. Liu, W. Ke, Z. Chen, L. Xiong and P. Qin, *Small*, 2017, **13**, 2.
21 G. Yang, H. Tao, P. Qin, W. Ke and G. Fang, *J. Mater. Chem. A*, 2016, **4**, 3970–3990.
22 H. Li, W. Shi, W. Huang, E.-P. Yao, J. Han, Z. Chen, S. Liu, Y. Shen, M. Wang and Y. Yang, *Nano Lett.*, 2017, **17**, 2328–2335.
23 J. H. Huang, M. A. Ibrahem and C. W. Chu, *Prog. Photovoltaics*, 2015, **23**, 1017–1024.
24 J.-H. Huang, H.-Y. Wei, K.-C. Huang, C.-L. Chen, R.-R. Wang, F.-C. Chen, K.-C. Ho and C.-W. Chu, *Energy Environ. Sci.*, 2010, **3**, 654–658.
25 J. Jiang, Z. Jin, J. Lei, Q. Wang, X. Zhang, J. Zhang, F. Gao and S. F. Liu, *J. Mater. Chem. A*, 2017, **5**, 9514–9522.
26 H. B. Kim, I. Im, Y. Yoon, S. Do Sung, E. Kim, J. Kim and W. I. Lee, *J. Mater. Chem. A*, 2015, **3**, 9264–9270.
27 Y. Ogomi, A. Morita, S. Tsukamoto, T. Saitho, Q. Shen, T. Toyoda, K. Yoshino, S. S. Pandey, T. Ma and S. Hayase, *J. Phys. Chem. C*, 2014, **118**, 16651–16659.
28 Y. Shih, L. Wang, H. Hsieh and K. Lin, *J. Mater. Chem. A*, 2015, **3**, 9133–9136.
29 L. Zuo, Z. Gu, T. Ye, W. Fu, G. Wu, H. Li and H. Chen, *J. Am. Chem. Soc.*, 2015, **137**, 2674–2679.
30 J. Cao, J. Yin, S. Yuan, Y. Zhao, J. Li and N. Zheng, *Nanoscale*, 2015, **7**, 9443–9447.
31 Z. Zhu, J. Ma, Z. Wang, C. Mu, Z. Fan, L. Du, Y. Bai, L. Fan, H. Yan and D. L. Phillips, *J. Am. Chem. Soc.*, 2014, **136**, 3760–3763.
32 K. Wojciechowski, S. D. Stranks, A. Abate, G. Sadoughi, A. Sadhanala, N. Kopidakis, G. Rumbles, C.-Z. Li, R. H. Friend and A. K.-Y. Jen, *ACS Nano*, 2014, **8**, 12701–12709.
33 Z. Li, C. Xiao, Y. Yang, S. P. Harvey, D. H. Kim, J. A. Christians, M. Yang, P. Schulz, S. U. Nanayakkara and C.-S. Jiang, *Energy Environ. Sci.*, 2017, **10**, 1234–1242.
34 Y. Wu, X. Yang, H. Chen, K. Zhang, C. Qin, J. Liu, W. Peng, A. Islam, E. Bi and F. Ye, *Appl. Phys. Express*, 2014, **7**, 052301.
35 A. Yella, L.-P. Heiniger, P. Gao, M. K. Nazeeruddin and M. Grätzel, *Nano Lett.*, 2014, **14**, 2591–2596.
36 L. Cojocaru, S. Uchida, Y. Sanehira, J. Nakazaki, T. Kubo and H. Segawa, *Chem. Lett.*, 2015, **44**, 674–676.
37 J. T.-W. Wang, J. M. Ball, E. M. Barea, A. Abate, J. A. Alexander-Webber, J. Huang, M. Saliba, I. Mora-Sero, J. Bisquert and H. J. Snaith, *Nano Lett.*, 2013, **14**, 724–730.
38 K. Wojciechowski, M. Saliba, T. Leijtens, A. Abate and H. J. Snaith, *Energy Environ. Sci.*, 2014, **7**, 1142–1147.
39 H. Zhou, Q. Chen, G. Li, S. Luo, T.-b. Song, H.-S. Duan, Z. Hong, J. You, Y. Liu and Y. Yang, *Science*, 2014, **345**, 542–546.
40 P. Vivo, A. Ojanperä, J.-H. Smått, S. Sandén, S. G. Hashmi, K. Kaunisto, P. Ihalainen, M. T. Masood, R. Österbacka and P. D. Lund, *Org. Electron.*, 2017, **41**, 287–293.
41 T. Hu, F. Li, K. Yuan and Y. Chen, *ACS Appl. Mater. Interfaces*, 2013, **5**, 5763–5770.
42 H. Yanagi, S. Chen, P. A. Lee, K. W. Nebesny, N. R. Armstrong and A. Fujishima, *J. Phys. Chem.*, 1996, **100**, 5447–5451.
43 Q. Jiang, L. Zhang, H. Wang, X. Yang, J. Meng, H. Liu, Z. Yin, J. Wu, X. Zhang and J. You, *Nat. Energy*, 2016, **2**, 16177.
44 S. H. Kang, K. Song, J. Jung, M. R. Jo and Y.-M. Kang, *J. Mater. Chem. A*, 2014, **2**, 19660–19664.
45 J.-H. Im, I.-H. Jang, N. Pellet, M. Grätzel and N.-G. Park, *Nat. Nanotechnol.*, 2014, **9**, 927–932.
46 X. Chen, L. J. Tang, S. Yang, Y. Hou and H. G. Yang, *J. Mater. Chem. A*, 2016, **4**, 6521–6526.
47 C. Tao, S. Neutzner, L. Colella, S. Marras, A. R. S. Kandada, M. Gandini, M. De Bastiani, G. Pace, L. Manna and M. Caironi, *Energy Environ. Sci.*, 2015, **8**, 2365–2370.
48 D. Yang, X. Zhou, R. Yang, Z. Yang, W. Yu, X. Wang, C. Li, S. F. Liu and R. P. Chang, *Energy Environ. Sci.*, 2016, **9**, 3071–3078.
49 R. H. Bube, *J. Appl. Phys.*, 1962, **33**, 1733–1737.
50 A. Poglitsch and D. Weber, *J. Chem. Phys.*, 1987, **87**, 6373–6378.
51 Y. Shao, Z. Xiao, C. Bi, Y. Yuan and J. Huang, *Nat. Commun.*, 2014, **5**, 5784.
52 T. Handa, D. M. Tex, A. Shimazaki, A. Wakamiya and Y. Kanemitsu, *J. Phys. Chem. Lett.*, 2017, **8**, 954–960.
53 Z. Liu, T. Shi, Z. Tang, B. Sun and G. Liao, *Nanoscale*, 2016, **8**, 7017–7023.
54 F. Zhang, X. Yang, M. Cheng, W. Wang and L. Sun, *Nano Energy*, 2016, **20**, 108–116.